Motion Artifact Reduction in Ambulatory Electrocardiography Using Inertial Measurement Units and Kalman Filtering

Roland Hostettler, Tuomas Lumikari, Lauri Palva, Tuomo Nieminen,
Simo Särkkä

Motion Artifact Reduction in Ambulatory Electrocardiography using Inertial Measurement Units and Kalman Filtering

Roland Hostettler*, Tuomas Lumikari†, Lauri Palva*, Tuomo Nieminen‡, and Simo Särkkä*

*Department of Electrical Engineering and Automation, Aalto University, Espoo, Finland
E-Mail: { roland.hostettler, lauri.palva, simo.sarkka }@aalto.fi
†Department of Neurology, Helsinki University Central Hospital, Helsinki, Finland
E-Mail: tuomas.lumikari@helsinki.fi
‡Department of Internal Medicine, South Karelia Central Hospital, University of Helsinki
and Helsinki University Central Hospital, Helsinki, Finland
E-Mail: tuomo.vm.nieminen@helsinki.fi

Abstract—**Electrocardiography (ECG) using lightweight and inexpensive ambulatory ECG devices makes it possible to monitor patients during their daily activities and can give important insight in arrhythmias and other cardiac diseases. However, everyday activities cause several kinds of motion artifacts which deteriorate the ECG quality and thus complicate both automated and manual ECG analysis. In this paper, we discuss some of the challenges associated with long-term ambulatory ECG and propose a baseline wander compensation algorithm based on inertial measurement units (IMUs) attached to each ECG electrode. The IMUs are used for estimating the local electrode motion which in turn is used as the reference signal for baseline wander reduction. We evaluate the proposed algorithm on data gathered in clinical trials and show that the baseline wander is successfully removed, without compromising the ECG's morphology.**

Index Terms—**Electrocardiography, signal reconstruction, Kalman filters, biomedical signal processing, inertial measurement units.**

I. Introduction

Ambulatory electrocardiography (ECG) devices facilitate cardiac monitoring of patients during their daily activities outside clinical settings. This enables the detection of abnormal cardiac cycles and arrhythmias that may only occur under certain circumstances or very sporadically [1], [2]. An example of such an arrhythmia is atrial fibrillation, which bears a 5-fold risk of ischaemic stroke if the patient is not anticoagulated. Multiple trials using a variety of ECG devices to reveal hidden AF after a stroke have been conducted [3], [4].

Ambulatory ECG devices normally provide measurements from up to three ECG leads, can measure continuously for up to several weeks, and their small size and weight only cause minimal discomfort to the patient. However, ambulatory ECG monitoring also poses significant challenges. For example, at a heart rate of $80\,\mathrm{bpm}$, each day of ECG recordings contains in the order of $115\,200$ individual cardiac cycles. Clearly, a cardiologist is unable to screen that vast amount of data, not even for a single patient. Hence, automated classification

methods that reliably detect abnormal cardiac cycles of interest are required [1], [2]. This task is complicated by several external disturbances such as 1) power line interference that induces a $50\,\mathrm{Hz}$ (or $60\,\mathrm{Hz}$) oscillation, 2) electromyographic (EMG) broadband disturbances due to action potentials in the nearby muscle cells, and 3) changes in the voltage across the electrode-skin interface due to electrode motion which causes so-called baseline wander [5], [6]. In this paper, we consider disturbances of the third type.

Electrode motion typically manifests as a low-frequency baseline wander. Unfortunately, its spectrum may overlap with the ECG signal's spectrum itself and thus, for example high-pass filtering of the ECG signal removes important information and is not appropriate to remove the baseline wander [5], [6]. Several different approaches have been proposed for removing this type of motion artifacts and they can roughly be divided into two approaches: 1) Methods based on the ECG signal alone and 2) methods that use a combination of the ECG signal and other measurements. The former approach includes, for example, signal model-based methods [7], [8], methods that decompose the ECG signal using independent component analysis [9], [10], circuit models describing the electrode-skin interface [11], [12], artificial neural networks [13], or approaches based on the assumption that the ECG morphology does not change significantly between consecutive cardiac cycles, which can be formulated as a high-dimensional, non-parametric state space model that can be used together with Kalman filtering [14]. Methods that combine the ECG signal with other measurements typically make use of additional sensors such as accelerometers, strain gauges, or magnetometers. Accelerometer-based approaches use different types of accelerometers (e.g. one- to three-axis accelerometers, with different placements on the body, etc.) together with adaptive filtering approaches such as recursive least squares or least mean squares filtering with the raw accelerometer signal as the reference signal [9], [15]–[17].

In this paper, we discuss some of the challenges that arise

in motion artifact compensation as well as the measurement setup and clinical trials used in our research. Furthermore, we propose a baseline wander compensation method based on local electrode motion estimation and Kalman filtering using commercially off the shelf inertial measurement units (IMUs) and magnetometers. The proposed method borrows ideas from inertial navigation [18]–[21] and in contrast to the existing methods, it is invariant to the sensor orientation since it estimates the full 3D short term sensor motion relative to its stationary position in the common global coordinate system. Additionally, the proposed approach is based on a setup that makes use of one sensor per electrode (i.e., two sensors per lead) that measure the corresponding lead's electrodes' motion, rather than just an individual sensor.

The remainder of this paper is organized as follows. Section II introduces the experimental setup and discusses the clinical trials as well as the challenges in motion artifact reduction. This is followed by the baseline wander reduction method in Section III. The evaluation of the proposed method on real data is provided in Section IV and some concluding remarks are given in Section V.

II. EXPERIMENTAL SETUP AND CLINICAL TRIALS

In this section, we describe the measurement setup as well as the clinical trials, followed by a brief analysis of the experiments and an illustration and discussion of the motion artifacts in the ECG signal.

A. Experimental Setup

The proposed measurement setup is illustrated in Fig. 1. We use a three-lead ambulatory ECG device (Faros 360, Bittium Biosignals, Oulu, Finland) where the five electrodes form the leads I (R/RA to L/LA), II (R/RA to F/LL), and V1 (CV to F/LL), with the reference electrode integrated in the ECG device. In addition to the ECG channels, the ambulatory ECG device also contains an integrated accelerometer, which is used for synchronizing the system clocks (see below). Furthermore, motion sensors (MetaMotion C, mbientlab, San Francisco, CA) are firmly attached on top of each of the electrodes. The motion sensors consist of an inertial measurement unit (IMU; BMI160, Bosch Sensortec, Reutlingen, Germany) and a magnetometer (BMM150, Bosch Sensortec, Reutlingen, Germany) and log the measurement data to the internal memory. For simplicity, we will refer to the complete motion sensors including the magnetometer as the "IMUs" for the remainder of this paper. Note that this kind of setup is not readily suitable for long-term ambulatory ECG monitoring due to the many separate components. Instead, a more integrated solution would be required. However, for our purpose of controlled clinical trials and algorithm development, this is not a concern.

During the trials, each of the ECG channels is sampled at $1000\,\mathrm{Hz}$, the IMUs' accelerometers and gyroscopes are sampled at $100\,\mathrm{Hz}$, and the magnetometer is sampled at $25\,\mathrm{Hz}$. In order to synchronize the clocks, a heel drop motion is performed before each trial, and the relative sensor delays are estimated using the cross-correlation of the accelerometer signals.
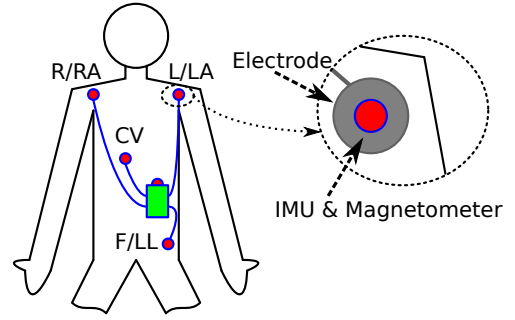

Fig. 1. Illustration of the experimental setup: A five-electrode, three-lead ambulatory ECG setup is used with four electrodes as marked and one reference electrode attached to ECG device (green box). A wireless IMU is attached on top of each electrode.

Using this setup, clinical trials (approved by the Ethics Committee of the Helsinki and Uusimaa Hospital District) with 20 subjects are performed. In the trials, each subject is asked to perform a set of seven motion sequences that are designed to simulate everyday tasks such as picking up items or moving during sleep. The motion sequences are:

1) Patient is lying on their back. Patient rolls on right side 90 degrees then returns to backside position.
2) Patient stands up from sitting position.
3) Patient is standing with upper limbs extended, then reaches floor without bending their knees.
4) Patient is starting with upper limbs rotated outwards and elbow joints at 90 degrees flexed. Keeping elbows flexed patient moves forearms together to the front.
5) Patient starts with upper limbs resting on sides, elbow joints extended. Keeping elbows extended, patient raises upper limbs above head forming a 180 degrees angle.
6) Patient starts with elbows flexed at 90 degrees, forearms touching in front, patient rotates upper body laterally on right side, returns to front, then left side and returns to front.
7) Patient walks in staircase, arms freely moving.

Each of these motions is performed twice before the subject moves on to the next motion.

B. Measurement Assessment

Two examples of the measured ECG and accelerometer signals are shown in Fig. 2 and Fig. 3. Fig. 2 shows the measured signals when one of the subjects performed motion sequence 3. It is clear that at the onset of the motion (around $t \approx 4\,\mathrm{s}$; c.f. the accelerometer signals in the middle and bottom panels), baseline wander is observed in the ECG signal (the deviations of the ECG signal's offset from zero). Furthermore, the ECG is also affected by broadband EMG noise due to muscle contractions during the bending motion (between $t \approx 5\,\mathrm{s}$ and $t \approx 8\,\mathrm{s}$ as well as between $t \approx 12\,\mathrm{s}$ and $t \approx 15\,\mathrm{s}$). The accelerometer measurements clearly indicate the change in pose (change in offset in all axes for both sensors) and also the motion itself (small superimposed accelerations). Note that after the motion is completed (after $t \approx 15\,\mathrm{s}$), the baseline

Fig. 2. Example lead II ECG (top), R/RA accelerometer (middle), and F/LL accelerometer (bottom) signals measured during motion sequence 3.
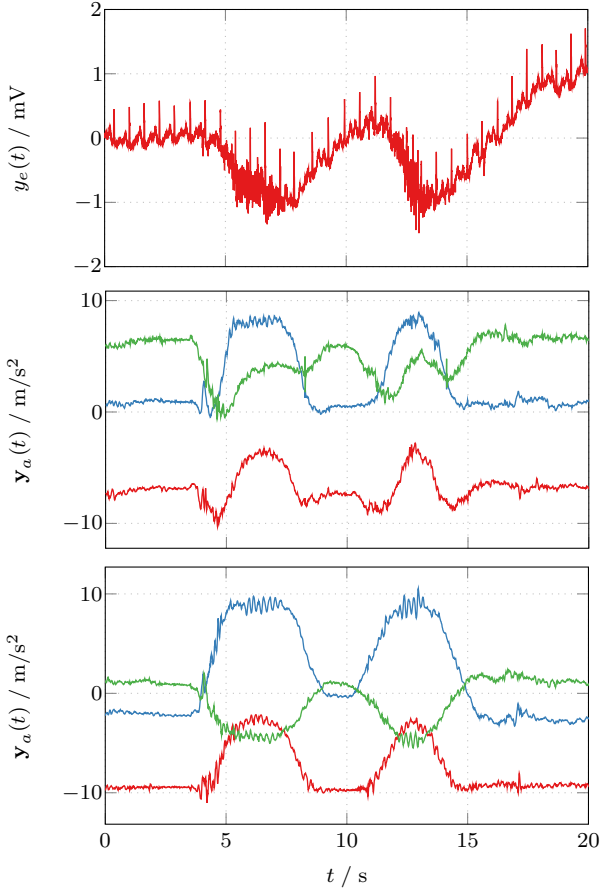

Fig. 3. Example lead II ECG (top), R/RA accelerometer (middle), and F/LL accelerometer (bottom) signals measured during motion sequence 4.

does not revert to zero immediately. This is mainly because it takes some time for the electrode-skin interface to return to steady-state after the disturbance.

Fig. 3 shows the lead II ECG together with the accelerations measured for the R/RA (middle) and F/LL (bottom) electrodes during motion sequence 4 for a different subject. In this case, the ECG baseline wander is not as distinctive as in the previous example (top), indicating less electrode motion. On the other hand, the EMG noise is much stronger (between $t \approx 2\,\text{s}$ and $t \approx 4\,\text{s}$ as well as between $t \approx 7\,\text{s}$ and $t \approx 9\,\text{s}$). This is possibly caused by the fact that this motion involves a much stronger contraction of the deltoid and pectoralis muscles that are close to the R/RA electrode. The accelerometer signals show that there is no significant change in attitude for either electrode (note that changes in attitude around the vertical axis can not be sensed using an accelerometer alone, see, e.g. [22]). The motion itself, however, can be clearly seen in both accelerometers.

These two examples illustrate two of the major challenges faced in ECG denoising. Unfortunately, it is hard to quantify or even analytically model these disturbances as they may vary not only between subjects but also between repetitions.
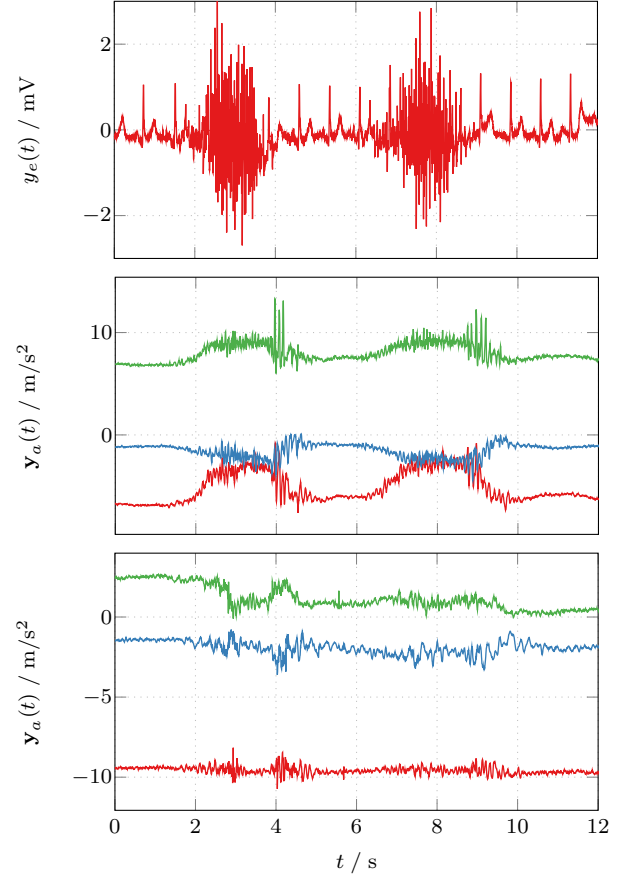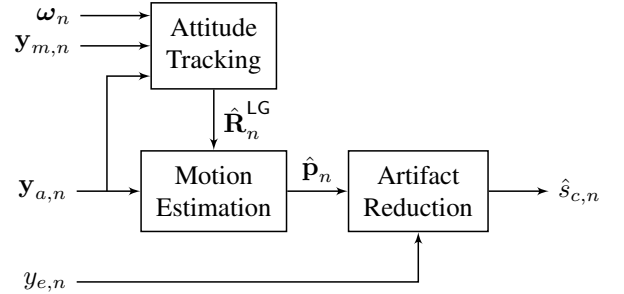

Fig. 4. Illustration of the motion artifact reduction algorithm.

III. MOTION ARTIFACT REDUCTION

The proposed motion artifact reduction method uses an estimate of the short term electrode motion relative to its stationary position as a reference signal. The latter is estimated by using an attitude tracker to transform the measured acceleration to global coordinates, followed by using inertial navigation together with stationarity detection and pseudo-position updates. The general algorithm structure is outlined in Fig. 4 and each of the steps is discussed in more detail in the following sections.

A. Attitude Tracking

The first step is to estimate the attitude of each of the IMUs. We achieve this by tracking the gravity and magnetic field vectors in the IMUs local coordinate frame (denoted by the superscript L) and then estimating the attitude matrix of the IMU.

At time t_n, the measured acceleration $\mathbf{y}_{a,n} \triangleq \mathbf{y}_a(t_n)$ is given by

$$\mathbf{y}_{a,n} = \mathbf{g}_n^{\mathsf{L}} + \mathbf{a}_n^{\mathsf{L}} + \mathbf{w}_{a,n}, \tag{1}$$

where $\mathbf{g}_n^{\mathsf{L}}$ denotes the (negative) gravity vector in the IMU's local coordinate system, $\mathbf{a}_n^{\mathsf{L}}$ is the body's acceleration, and $\mathbf{w}_{a,n} \sim \mathcal{N}(\mathbf{0}, \mathbf{C}_a)$ is the measurement noise. Similarly, the measurement model for the magnetometer can be written as

$$\mathbf{y}_{m,n} = \mathbf{m}_n^{\mathsf{L}} + \mathbf{b}_m + \mathbf{w}_{m,n}, \tag{2}$$

where $\mathbf{m}_n^{\mathsf{L}}$ is the magnetic field vector in the IMU's local coordinate system, $\mathbf{b}_m$ is the magnetometer bias, and $\mathbf{w}_{m,n} \sim \mathcal{N}(\mathbf{0}, \mathbf{C}_m)$ is the measurement noise. (Note that we assume the magnetometer bias to be constant and estimate it using the conventional sphere fitting calibration approach, see [23], [24].)

Furthermore, the dynamic model for rotations of the local gravity and magnetic field vectors can be written as [19]

$$\mathbf{r}_n = \mathbf{A}(\boldsymbol{\omega}_n)\mathbf{r}_{n-1} + \mathbf{v}_n, \tag{3}$$

where

$$\mathbf{A}(\boldsymbol{\omega}_n) = \mathbf{I}_3 + \sin(|\boldsymbol{\omega}_n|\Delta t)\frac{[-\boldsymbol{\omega}_n]_\times}{|\boldsymbol{\omega}_n|}$$
$$+ (1 - \cos(|\boldsymbol{\omega}_n|\Delta t))\frac{[-\boldsymbol{\omega}_n]_\times^2}{|\boldsymbol{\omega}_n|^2},$$

$\Delta t_n = t_n - t_{n-1}$ is the sampling time, $\mathbf{r}_n$ is either $\mathbf{g}_n^{\mathsf{L}}$ or $\mathbf{m}_n^{\mathsf{L}}$, $\boldsymbol{\omega}_n$ is the angular velocity as measured by the gyroscope, $[\cdot]_\times$ denotes the cross product matrix, and $\mathbf{v}_n \sim \mathcal{N}(\mathbf{0}, \mathbf{C}_v)$ is the process noise.

Then, by using the dynamic model (3) for both the gravity and the magnetic field vector, together with the accelerometer and magnetometer models (1)–(2), we can track both $\mathbf{g}_n^{\mathsf{L}}$ and $\mathbf{m}_n^{\mathsf{L}}$. To this end, we use the robust Kalman filtering and smoothing algorithm introduced in [19] and shown in Algorithm 1, which automatically adapts the measurement noise covariance if significant body acceleration is detected. The algorithm is used for tracking the gravity and magnetic field vector separately (i.e., the same algorithm is applied to both problems independently). Note that in Algorithm 1, α_0 denotes the covariance adaption factor, γ the outlier detection threshold, and τ the covariance adaption time constant. Furthermore, the superscript j on $\mathbf{y}_{j,n}$ and $\mathbf{C}_j$ is either a for the accelerometer or m for the magnetometer, see (1)–(2). Finally, note that the algorithm parameters (e.g., α_0 and γ) may be different for gravity tracking and magnetic field vector tracking.

This yields the estimated gravity and magnetic field vectors $\hat{\mathbf{g}}_n^{\mathsf{L}}$ and $\hat{\mathbf{m}}_n^{\mathsf{L}}$, respectively. From these, we can readily estimate the attitude of the IMU in the global east-north-up (ENU) coordinate system as follows. First, an estimate of the normal

---

Algorithm 1 Robust Reference Vector Tracking Step [19]

1: Prediction:
$$\hat{\mathbf{r}}_n^- = \mathbf{A}(\boldsymbol{\omega}_n)\hat{\mathbf{r}}_{n-1}$$
$$\mathbf{C}_{\mathbf{r},n}^- = \mathbf{A}(\boldsymbol{\omega}_n)\mathbf{C}_{\mathbf{r},n-1}\mathbf{A}(\boldsymbol{\omega}_n)^{\mathsf{T}} + \mathbf{C}_v$$

2: Measurement covariance adaption:
$$\alpha_n = \exp(-\Delta t_n/\tau)\alpha_{n-1}$$
$$\boldsymbol{\nu}_n = \mathbf{y}_{j,n} - \hat{\mathbf{r}}_n^-$$
$$\mathbf{S}_n = \mathbf{C}_{\mathbf{r},n}^- + \mathbf{C}_j + \alpha_n\mathbf{I}_3$$

3: **if** $\boldsymbol{\nu}_n^{\mathsf{T}}\mathbf{S}_n^{-1}\boldsymbol{\nu}_n > \gamma$ **then**
4:     Set
$$\alpha_n = \alpha_0$$
$$\mathbf{S}_n = \mathbf{C}_{\mathbf{r},n}^- + \mathbf{C}_j + \alpha_n\mathbf{I}_3$$

5: **end if**
6: Measurement update:
$$\mathbf{K}_n = \mathbf{C}_{\mathbf{r},n}^-\mathbf{S}_n^{-1}$$
$$\hat{\mathbf{r}}_n = \hat{\mathbf{r}}_n^- + \mathbf{K}_n\boldsymbol{\nu}_n$$
$$\mathbf{C}_{\mathbf{r},n} = \mathbf{C}_{\mathbf{r},n}^- - \mathbf{K}_n\mathbf{S}_n\mathbf{K}_n^{\mathsf{T}}$$

---

reference vector $\mathbf{e}_n^{\mathsf{z,L}}$ is readily obtained from the local gravity estimate as

$$\hat{\mathbf{e}}_n^{\mathsf{z,L}} = \frac{\hat{\mathbf{g}}_n^{\mathsf{L}}}{|\hat{\mathbf{g}}_n^{\mathsf{L}}|}. \tag{4}$$

Second, the east (x) reference vector is found from the normalized cross product between the magnetic field vector and the normal reference vector and is given by

$$\hat{\mathbf{e}}_n^{\mathsf{x,L}} = \frac{\hat{\mathbf{m}}_n^{\mathsf{L}} \times \hat{\mathbf{e}}_n^{\mathsf{z,L}}}{|\hat{\mathbf{m}}_n^{\mathsf{L}} \times \hat{\mathbf{e}}_n^{\mathsf{z,L}}|}. \tag{5}$$

Third, the remaining reference vector (north; y) is readily found from the cross product of $\hat{\mathbf{e}}_n^{\mathsf{z,L}}$ and $\hat{\mathbf{e}}_n^{\mathsf{x,L}}$ to be

$$\hat{\mathbf{e}}_n^{\mathsf{y,L}} = \hat{\mathbf{e}}_n^{\mathsf{z,L}} \times \hat{\mathbf{e}}_n^{\mathsf{x,L}}. \tag{6}$$

Eqs. (4)–(6) then yield an estimate of the IMUs attitude (rotation matrix) which is given by

$$\hat{\mathbf{R}}_n^{\mathsf{LG}} = \begin{bmatrix} \hat{\mathbf{e}}_n^{\mathsf{x,L}} & \hat{\mathbf{e}}_n^{\mathsf{y,L}} & \hat{\mathbf{e}}_n^{\mathsf{z,L}} \end{bmatrix}. \tag{7}$$

B. Electrode Motion Estimation

Given the attitude of each IMU, we estimate the relative motion of each IMU in the global coordinate system as follows. First, the IMU acceleration is estimated from the raw acceleration measurements $\mathbf{y}_{a,n}$, the estimated local gravity vector $\hat{\mathbf{g}}_n^{\mathsf{L}}$, and the attitude $\hat{\mathbf{R}}_n^{\mathsf{LG}}$ as

$$\hat{\mathbf{a}}_n = (\hat{\mathbf{R}}_n^{\mathsf{LG}})^{\mathsf{T}}(\mathbf{y}_{a,n} - \hat{\mathbf{g}}_n^{\mathsf{L}}), \tag{8}$$

which yields

$$\hat{\mathbf{a}}_n \sim \mathcal{N}(\mathbf{a}_n, \mathbf{C}_{\hat{\mathbf{a}},n}), \tag{9}$$

with

$$\mathbf{C}_{\hat{\mathbf{a}},n} = (\hat{\mathbf{R}}_n^{\mathsf{LG}})^{\mathsf{T}}(\mathbf{C}_{\hat{\mathbf{g}},n} + \mathbf{C}_a)\hat{\mathbf{R}}_n^{\mathsf{LG}}, \tag{10}$$

and $\mathbf{C}_{\hat{\mathbf{g}},n}$ is the covariance matrix of $\hat{\mathbf{g}}_n^{\mathsf{L}}$. Next, we use the estimated global acceleration to estimate the relative 3D motion of the IMUs using the standard inertial navigation model [22]

$$\mathbf{x}_n = \mathbf{F}_n\mathbf{x}_{n-1} + \mathbf{L}_n\hat{\mathbf{a}}_n. \tag{11}$$

where

$$\mathbf{x}_n = \begin{bmatrix} \mathbf{p}_n \\ \mathbf{v}_n \end{bmatrix}, \ \mathbf{F}_n = \begin{bmatrix} 1 & \Delta t_n \\ 0 & 1 \end{bmatrix} \otimes \mathbf{I}_3, \ \mathbf{L}_n = \begin{bmatrix} \frac{(\Delta t_n)^2}{2} \\ \Delta t_n \end{bmatrix} \otimes \mathbf{I}_3,$$

$\mathbf{p}_n$ denotes the electrode's position, $\mathbf{v}_n$ its velocity, and $\otimes$ is the Kronecker product.

To prevent divergence of the double integration (11) caused by gravity leaking and accelerometer bias, we use detection of stationary phases and pseudo measurement updates when such phases are detected. This is a common approach to stabilize foot-mounted or hand-held inertial navigation, see, for example, [18], [25].

In order to detect the stationary phases, we use a statistical test similar to [26]: Considering a sliding window of length M, we calculate the mean acceleration

$$\bar{\mathbf{a}}_n = \frac{1}{M}\sum_{m=0}^{M-1}\hat{\mathbf{a}}_{n-m}, \tag{12}$$

which, under the null (i.e. stationary) hypothesis is distributed according to

$$\bar{\mathbf{a}}_n \sim \mathcal{N}(\mathbf{0}, \mathbf{C}_{\bar{\mathbf{a}},n}) \tag{13}$$

with

$$\mathbf{C}_{\bar{\mathbf{a}},n} = \frac{1}{M^2}\sum_{m=0}^{M-1}\mathbf{C}_{\hat{\mathbf{a}},n-m}. \tag{14}$$

Then, the test statistic

$$\rho_n = \bar{\mathbf{a}}_n^{\mathsf{T}}\mathbf{C}_{\bar{\mathbf{a}},n}^{-1}\bar{\mathbf{a}}_n \tag{15}$$

is distributed according to a χ^2 distribution with three degrees of freedom. Hence, we choose a threshold κ such that $\Pr\{\rho_n \leq \kappa\} = \alpha$ under the null hypothesis and deem the IMU to be stationary whenever $\rho_n \leq \kappa$.

Since we are only interested in the short term motion of the electrode relative to its stationary position, we do a zero position pseudo measurement update (rather than a zero velocity update common in, for example, foot-mounted inertial navigation [18]). In practice, this means that we do a pseudo measurement update according to the measurement model

$$\mathbf{y}_{p,n} = \underbrace{\begin{bmatrix} \mathbf{I}_3 & \mathbf{0} \end{bmatrix}}_{\triangleq\mathbf{G}}\mathbf{x}_n + \mathbf{w}_{p,n}, \tag{16}$$

with $\mathbf{y}_{p,n} = \begin{bmatrix} 0 & 0 & 0 \end{bmatrix}^{\mathsf{T}}$ and $\mathbf{w}_{p,n} \sim \mathcal{N}(\mathbf{0}, \mathbf{C}_p)$.

We can now again use a (modified) Kalman filter using the dynamic model (11) with the input (8), and conditional measurement updates (16), which yields the algorithm shown in Algorithm 2.

Algorithm 2 Motion Estimation Step

1: Estimate $\hat{\mathbf{a}}_n$ and $\mathbf{C}_{\hat{\mathbf{a}},n}$ using (8) and (10)
2: Prediction:

$$\hat{\mathbf{x}}_n^- = \mathbf{F}_n\hat{\mathbf{x}}_{n-1} + \mathbf{L}_n\hat{\mathbf{a}}_n$$
$$\mathbf{C}_{\hat{\mathbf{x}},n}^- = \mathbf{F}_n\mathbf{C}_{\hat{\mathbf{x}},n-1}\mathbf{F}_n^{\mathsf{T}} + \mathbf{L}_n\mathbf{C}_{\hat{\mathbf{a}},n}\mathbf{L}_n^{\mathsf{T}}$$

3: Stationarity detection:

$$\bar{\mathbf{a}}_n = \bar{\mathbf{a}}_{n-1} + \frac{1}{M}\left(\hat{\mathbf{a}}_n - \hat{\mathbf{a}}_{n-M}\right)$$
$$\mathbf{C}_{\bar{\mathbf{a}},n} = \mathbf{C}_{\bar{\mathbf{a}},n-1} + \frac{1}{M^2}\left(\mathbf{C}_{\hat{\mathbf{a}},n} - \mathbf{C}_{\hat{\mathbf{a}},n-M}\right)$$
$$\rho_n = \bar{\mathbf{a}}_n^{\mathsf{T}}\mathbf{C}_{\bar{\mathbf{a}},n}^{-1}\bar{\mathbf{a}}_n$$

4: **if** $\rho_n \leq \kappa$ **then**
5:     Pseudo measurement update:

$$\hat{\mathbf{p}}_n^- = \mathbf{G}\hat{\mathbf{x}}_n^-$$
$$\mathbf{S}_n = \mathbf{G}\mathbf{C}_{\hat{\mathbf{x}},n}^-\mathbf{G}^{\mathsf{T}} + \mathbf{C}_p$$
$$\mathbf{K}_n = \mathbf{C}_{\hat{\mathbf{x}},n}^-\mathbf{G}^{\mathsf{T}}\mathbf{S}_n^{-1}$$
$$\hat{\mathbf{x}}_n = \hat{\mathbf{x}}_n^- + \mathbf{K}_n(\mathbf{0} - \hat{\mathbf{p}}_n^-)$$
$$\mathbf{C}_{\hat{\mathbf{x}},n} = \mathbf{C}_{\hat{\mathbf{x}},n}^- - \mathbf{K}_n\mathbf{S}_n\mathbf{K}_n^{\mathsf{T}}$$

6: **else**
7:     Set

$$\hat{\mathbf{x}}_n = \hat{\mathbf{x}}_n^-$$
$$\mathbf{C}_{\hat{\mathbf{x}},n} = \mathbf{C}_{\hat{\mathbf{x}},n}^-$$

8: **end if**

C. Motion Artifact Reduction

Finally, the estimated local position $\hat{\mathbf{p}}_n$ is used as the reference signal for motion artifact reduction. The ECG signal for any given lead is modeled as a superposition of the cardiac signal $s_{c,n}$ and the baseline wander disturbance $s_{d,n}$. This yields the measurement model

$$y_{e,n} = s_{c,n} + s_{d,n} + w_{e,n}, \tag{17}$$

where $w_{e,n} \sim \mathcal{N}(0, C_e)$ is the measurement noise.

We assume that the motion artifact component $s_{d,n}$ exhibits a time-varying correlation with the local motion of the electrode. Hence, we model $s_{d,n}$ as a filtered version of the lead's two electrodes' relative positions with time varying coefficients

$$s_{d,n} = \mathbf{H}_n\boldsymbol{\beta}_n \tag{18}$$

with

$$\mathbf{H}_n = \begin{bmatrix} 1 & \hat{\mathbf{p}}_{1,n}^{\mathsf{T}} & \cdots & \hat{\mathbf{p}}_{1,n-L+1}^{\mathsf{T}} & \hat{\mathbf{p}}_{2,n}^{\mathsf{T}} & \cdots & \hat{\mathbf{p}}_{2,n-L+1}^{\mathsf{T}} \end{bmatrix},$$

L is the filter length, and $\boldsymbol{\beta}_n$ is a $(3L+1) \times 1$ vector of filter coefficients. We model the latter as a slowly time-varying random walk, that is, according to the dynamic model

$$\boldsymbol{\beta}_n = \boldsymbol{\beta}_{n-1} + \mathbf{q}_n, \tag{19}$$

Algorithm 3 Motion Artifact Reduction Step

1: Prediction:

$$\hat{\boldsymbol{\beta}}_n^- = \hat{\boldsymbol{\beta}}_{n-1}$$
$$\mathbf{C}_{\hat{\boldsymbol{\beta}},n}^- = \mathbf{C}_{\hat{\boldsymbol{\beta}},n} + \mathbf{C}_q$$

2: Measurement update:

$$\hat{s}_{d,n} = \mathbf{H}_n\hat{\boldsymbol{\beta}}_n^-$$
$$S_n = \mathbf{H}_n\mathbf{C}_{\hat{\boldsymbol{\beta}},n}^-\mathbf{H}_n^\mathsf{T} + \tilde{C}_e$$
$$\mathbf{K}_n = \mathbf{C}_{\hat{\boldsymbol{\beta}},n}^-\mathbf{H}_n^\mathsf{T}S_n^{-1}$$
$$\hat{\boldsymbol{\beta}}_n = \hat{\boldsymbol{\beta}}_n^- + \mathbf{K}_n(y_{e,n} - \hat{s}_{d,n})$$
$$\mathbf{C}_{\hat{\boldsymbol{\beta}},n} = \mathbf{C}_{\hat{\boldsymbol{\beta}},n}^- - \mathbf{K}_nS_n\mathbf{K}_n^\mathsf{T}$$

3: Estimate ECG signal:

$$\hat{s}_{e,n} = y_{e,n} - \hat{s}_{d,n}$$

where $\mathbf{q}_n \sim \mathcal{N}(\mathbf{0}, \mathbf{C}_q)$ is the process noise. Furthermore, absorbing the ECG signal $s_{c,n}$ in (17) into the measurement uncertainty yields

$$y_{e,n} \approx \mathbf{H}_n\boldsymbol{\beta}_n + \tilde{w}_{e,n}, \tag{20}$$

where the measurement noise $\tilde{w}_{e,n}$ also includes the unmodeled ECG signal, which causes $\tilde{w}_{e,n}$ to be non-Gaussian. Nevertheless, we assume that $\tilde{w}_{e,n} \sim \mathcal{N}(0, \tilde{C}_e)$, where the increased measurement noise covariance accounts for the unmodeled ECG signal.

The model (19)–(20) again allows us to use a standard Kalman filter to estimate the coefficients $\boldsymbol{\beta}_n$ and, more importantly, the unknown disturbance $s_{d,n}$. The latter is obtained as the one step ahead prediction during the Kalman filter measurement update step and is given by

$$\hat{s}_{d,n} = \mathbf{H}_n\hat{\boldsymbol{\beta}}_n^-. \tag{21}$$

From (21), we finally obtain the estimate of the motion artifact reduced ECG signal for a single lead according to

$$\hat{s}_{c,n} = y_{e,n} - \hat{s}_{d,n}. \tag{22}$$

This yields the final step of the motion artifact reduction algorithm shown in Algorithm 3.

IV. RESULTS

In this section, the results of applying the motion compensation algorithm introduced in Sec. III to the experimental data gathered as discussed in Sec. II are shown. The parameters used in the algorithm are listed in Table I.

Fig. 5 shows the motion compensated signal after applying the proposed method to the example ECG signal in Fig. 2 (top). The comparison of the raw and processed signals shows that most of the baseline wander has successfully been removed. There is some slight baseline wander left, which could be removed by adjusting the compensation algorithm's parameters (in particular the process noise covariance of the

TABLE I
ALGORITHM PARAMETERS.

| Symbol	Description	Value
$\mathbf{C}_a$	Accelerometer noise covariance	$\mathbf{I}_3$
$\mathbf{C}_m$	Magnetometer noise covariance	$\mathbf{I}_3$
$\mathbf{C}_v$	Reference vector process noise covariance	$\Delta t_n\mathbf{I}_3$
α_0	Measurement noise adaption constant	1
γ	Outlier detection threshold	6
τ	Covariance adaption time constant	1
M	Stationarity detection sliding window length	100
κ	Stationarity detection threshold	7.8
$\mathbf{C}_p$	Position pseudo measurement noise covariance	1×10^{-3}
L	Filter length	15
$\mathbf{C}_q$	Filter coefficients process noise covariance	1×10^{-5}
$\tilde{C}_e$	ECG noise covariance	0.5
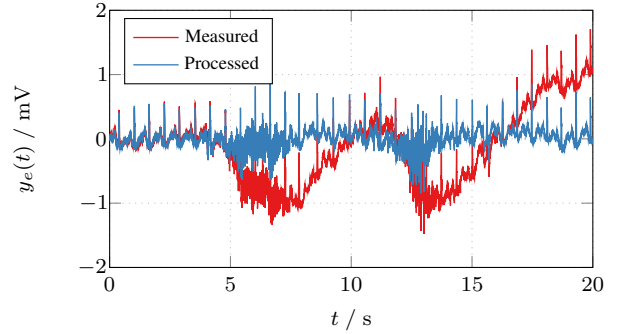
Fig. 5. Example of the raw and baseline wander compensated ECG signals for one subject during motion sequence 3 (lead II; the same as in Fig. 2).

coefficients $\boldsymbol{\beta}_n$). This would, however, also compromise the morphology of the individual ECG beats. It is also clear from Fig. 5 that the EMG noise is mostly unaffected by the motion compensation algorithm. This is in accordance with the common understanding of the broadband EMG disturbances having a spectrum different from the baseline wander [5], [6]. Furthermore, the R-peaks (the dominating peaks) are well preserved throughout the signal.

In addition, a close-up excerpt of the first 3 s of the signal in Fig. 5 is shown in Fig. 6. In this period, there are no significant motion artifacts (c.f. Fig. 2). Thus, the motion artifact reduction algorithm should not affect the estimated ECG signal and preserve the morphology. As Fig. 6 shows, this is the case: The processed signal is altered slightly (e.g. the R-peaks are slightly decreased), but the morphology is unaffected and the P-wave (the small peak immediately before the large peak), QRS complex (the bottom-peak-bottom sequence around the main peak), and T-wave (small peak following the main peak) are clearly visible (please refer to, for example, [27] for more details on the ECG morphology).

Finally, Fig. 7 shows another close-up example of the same signal, but this time for the period between 12 s and 15 s. During this phase, there are significant motion artifacts in the form of both baseline wander and EMG disturbances. Here, the baseline wander is successfully removed (the processed ECG signal is centered around zero) and visual comparison of the
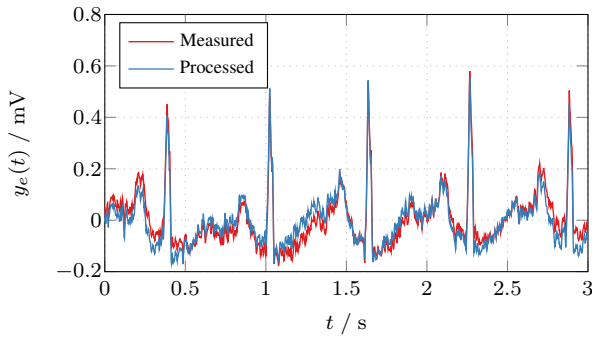
Fig. 6. Comparison of the measured and processed ECG during a period without motion artifacts.
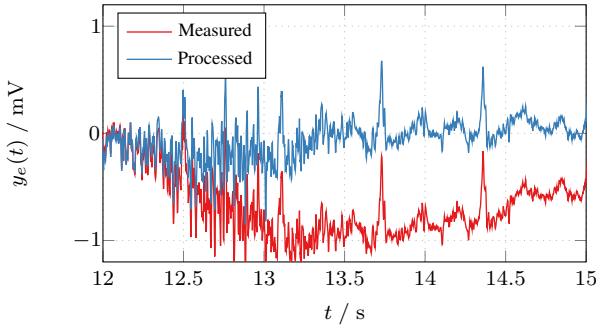

Fig. 7. Comparison of the measured and processed ECG during a period with motion artifacts.

raw and processed ECG shows that the cardiac cycles' features' are retained and no false features are introduced. The more detailed view here also shows that the EMG noise is indeed not affected by the compensation algorithm. Thus, cardiac cycles that are masked by the EMG noise are not recovered either.

V. Conclusions

In this paper, we have discussed the general challenges of ECG artifact removal as well as the measurement setup used in our research. Furthermore, we have presented an adaptive baseline wander compensation algorithm based on our measurement setup, which uses local sensor motion as the reference input. It has been shown that the proposed method successfully removes the baseline wander without altering the ECG morphology, which is one important step towards successful analysis by either a cardiologist or automated classification algorithms.

An important challenge that remains is that of removing, or at least detecting, EMG noise caused by muscle activity close to the electrodes. This is particularly challenging since compensation algorithms designed for this purpose may not alter existing or introduce new ECG features that are hidden in the noisy signals. Furthermore, future work will also investigate the performance improvement of both manual and automated ECG analysis for the de-noised ECG signals.

References

[1] C. Gumbinger, U. Krumsdorf, R. Veltkamp, W. Hacke, and P. Ringleb, "Continuous monitoring versus Holter ECG for detection of atrial fibrillation in patients with stroke," *European Journal of Neurology*, vol. 19, no. 2, pp. 253–257, 2012.

[2] M. Grond, M. Jauss, G. Hamann, E. Stark, R. Veltkamp, D. Nabavi, M. Horn, C. Weimar, M. Köhrmann, R. Wachter, L. Rosin, and P. Kirchhof, "Improved detection of silent atrial fibrillation using 72-hour Holter ECG in patients with ischemic stroke," *Stroke*, vol. 44, no. 12, 2013.

[3] P. A. Wolf, R. D. Abbott, and W. B. Kannel, "Atrial fibrillation as an independent risk factor for stroke: The Framingham study," *Stroke*, vol. 22, no. 8, pp. 983–988, 1991.

[4] D. Jabaudon, J. Sztajzel, K. Sievert, T. Landis, and R. Sztajzel, "Usefulness of ambulatory 7-day ECG monitoring for the detection of atrial fibrillation and flutter after acute stroke and transient ischemic attack," *Stroke*, vol. 35, no. 7, pp. 1647–1651, 2004.

[5] J. G. Webster, "Reducing motion artifacts and interference in biopotential recording," *IEEE Transactions on Biomedical Engineering*, vol. BME-31, no. 12, pp. 823–826, December 1984.

[6] K. T. Sweeney, T. E. Ward, and S. F. McLoone, "Artifact removal in physiological signals — practices and possibilities," *IEEE Transactions on Information Technology in Biomedicine*, vol. 16, no. 3, pp. 488–500, May 2012.

[7] P. E. McSharry, G. D. Clifford, L. Tarassenko, and L. A. Smith, "A dynamical model for generating synthetic electrocardiogram signals," *IEEE Transactions on Biomedical Engineering*, vol. 50, no. 3, pp. 289–294, March 2003.

[8] R. Sameni, M. B. Shamsollahi, C. Jutten, and G. D. Clifford, "A nonlinear Bayesian filtering framework for ECG denoising," *IEEE Transactions on Biomedical Engineering*, vol. 54, no. 12, pp. 2172–2185, Decenber 2007.

[9] M. Milanesi, N. Martini, N. Vanello, V. Positano, M. F. Santarelli, R. Paradiso, D. De Rossi, and L. Landini, "Multichannel techniques for motion artifacts removal from electrocardiographic signals," in *28th International Conference of the IEEE Engineering in Medicine and Biology Society*, August 2006, pp. 3391–3394.

[10] T. Pawar, S. Chaudhuri, and S. P. Duttagupta, "Body movement activity recognition for ambulatory cardiac monitoring," *IEEE Transactions on Biomedical Engineering*, vol. 54, no. 5, pp. 874–882, May 2007.

[11] S. Heuer, D. R. Martinez, S. Fuhrhop, and J. Ottenbacher, "Motion artefact correction for capacitive ECG measurement," in *IEEE Biomedical Circuits and Systems Conference*, November 2009, pp. 113–116.

[12] J. Ottenbacher and S. Heuer, "Motion artefacts in capacitively coupled ECG electrodes," in *World Congress on Medical Physics and Biomedical Engineering*, 2010, pp. 1059–1062.

[13] S. Poungponsri and X.-H. Yu, "An adaptive filtering approach for electrocardiogram (ECG) signal noise reduction using neural networks," *Neurocomputing*, vol. 117, pp. 206–213, 2013.

[14] R. Vullings, B. de Vries, and J. W. M. Bergmans, "An adaptive Kalman filter for ECG signal enhancement," *IEEE Transactions on Biomedical Engineering*, vol. 58, no. 4, pp. 1094–1103, April 2011.

[15] D. A. Tong, K. A. Bartels, and K. S. Honeyager, "Adaptive reduction of motion artifact in the electrocardiogram," in *24th International Conference of the IEEE Engineering in Medicine and Biology Society*, vol. 2, 2002, pp. 1403–1404.

[16] M. A. D. Raya and L. G. Sison, "Adaptive noise cancelling of motion artifact in stress ECG signals using accelerometer," in *24th International Conference of the IEEE Engineering in Medicine and Biology Society*, vol. 2, 2002, pp. 1756–1757.

[17] Y. Kishimoto, Y. Kutsuna, and K. Oguri, "Detecting motion artifact ECG noise during sleeping by means of a tri-axis accelerometer," in *29th International Conference of the IEEE Engineering in Medicine and Biology Society*, August 2007, pp. 2669–2672.

[18] J.-O. Nilsson, A. K. Gupta, and P. Händel, "Foot-mounted inertial navigation made easy," in *5th International Conference on Indoor Positioning and Indoor Navigation (IPIN)*, October 2014, pp. 24–29.

[19] S. Särkkä, V. Tolvanen, J. Kannala, and E. Rahtu, "Adaptive Kalman filtering and smoothing for gravitation tracking in mobile systems," in *6th International Conference on Indoor Positioning and Indoor Navigation*, October 2015.

[20] R. Hostettler and S. Särkkä, "IMU and magnetometer modeling for smartphone-based PDR," in *7th International Conference on Indoor Positioning and Indoor Navigation (IPIN)*, Alcalá de Henares, Spain, October 2016.

[21] M. Kok, J. D. Hol, and T. B. Schön, "Using inertial sensors for position and orientation estimation," *Foundations and Trends in Signal Processing*, vol. 11, no. 1–2, pp. 1–153, 2017.

[22] D. Titterton and J. Weston, *Strapdown Inertial Navigation Technology*, 2nd ed. The Institution of Engineering and Technology, 2004.

[23] R. Alonso and M. D. Shuster, "Attitude-independent magnetometer-bias determination: A survey," *Journal of the Astronautical Sciences*, vol. 50, no. 4, pp. 453–476, 2002.

[24] M. Kok and T. B. Schön, "Magnetometer calibration using inertial sensors," *IEEE Sensors Journal*, vol. 16, no. 14, pp. 5679–5689, July 2016.

[25] Z. Xiao, H. Wen, A. Markham, and N. Trigoni, "Robust pedestrian dead reckoning (R-PDR) for arbitrary mobile device placement," in *Indoor Positioning and Navigation (IPIN), 5th International Conference on*, October 2014, pp. 187–196.

[26] I. Skog, P. Händel, J.-O. Nilsson, and J. Rantakokko, "Zero-velocity detection — an algorithm evaluation," *IEEE Transactions on Biomedical Engineering*, vol. 57, no. 11, pp. 2657–2666, November 2010.

[27] J. G. Webster, *Medical Instrumentation: Application and Design*, 4th ed. Wiley, February 2009.